






RESEARCH ARTICLE | AUGUST 18 2023

## Altered blood rheology in multiwidth microchannels: Hematocrit and tonicity variation

C. Riera-Llobet ; L. Méndez-Mora  ; M. Cabello-Fusarés ; A. Hernández-Machado 



*Physics of Fluids* 35, 082017 (2023)

<https://doi.org/10.1063/5.0154713>



### Articles You May Be Interested In

A simple and low-cost paper-based device for simultaneous determination of hematocrit and hemoglobin levels in point-of-care settings

*Physics of Fluids* (December 2023)

Facile compliance-based pump for blood physiometer

*Physics of Fluids* (May 2024)

Interplay between size and softness in the vascular dynamics of microcarriers

*Physics of Fluids* (February 2023)



Physics of Fluids

Special Topics Open  
for Submissions

[Learn More](#)

# Altered blood rheology in multiwidth microchannels: Hematocrit and tonicity variation

Cite as: Phys. Fluids **35**, 082017 (2023); doi: [10.1063/5.0154713](https://doi.org/10.1063/5.0154713)

Submitted: 15 April 2023 · Accepted: 28 July 2023 ·

Published Online: 18 August 2023



View Online



Export Citation



CrossMark

C. Riera-Llobet,<sup>1</sup> L. Méndez-Mora,<sup>1,a)</sup> M. Cabello-Fusarés,<sup>2</sup> and A. Hernández-Machado<sup>1,2,3</sup>

## AFFILIATIONS

<sup>1</sup>Department of Condensed Matter Physics, University of Barcelona. Barcelona 08028, Spain

<sup>2</sup>Centre de Recerca Matemàtica, Universitat Autònoma de Barcelona, Bellaterra 08193, Spain

<sup>3</sup>Institute of Nanoscience and Nanotechnology (IN2UB), University of Barcelona, Barcelona 08028, Spain

<sup>a)</sup>Author to whom correspondence should be addressed: [lmendemo9.alumnes@ub.edu](mailto:lmendemo9.alumnes@ub.edu)

## ABSTRACT

We present a theoretical model for the characterization of the behavior of Newtonian and non-Newtonian fluids inside a microchannel with segments of different widths. This allows us to find the relation required to have collapsed viscosity curves for different fluids in just one experiment. Diverse experiments have been carried out with our setup. We consider different hematocrit concentration samples as well as samples of blood altered with different solutions in order to modify their tonicity. The data are acquired using microscale electronic detection of a fluid/air front advance. This will disclose different diseases that can be distinguished by the change in the normal rheological characteristics of blood or plasma. The results obtained demonstrate that using our setup and mathematical model, we can both distinguish blood with different concentrations of erythrocytes as well as discriminate when a same sample of blood is non-altered, altered with sodium chloride (NaCl) or de-ionized water (DIW), which emulates the abnormalities in the red blood cells of some pathologies. The results show that DIW causes blood to have more non-Newtonian behavior. On the other hand, NaCl causes the sample to become a hypertonic solution, causing the red blood cells to crenate, causing the blood to have a more Newtonian behavior.

© 2023 Author(s). All article content, except where otherwise noted, is licensed under a Creative Commons Attribution (CC BY) license (<http://creativecommons.org/licenses/by/4.0/>). <https://doi.org/10.1063/5.0154713>

## I. INTRODUCTION

Micro- and nanoscale fluidics is a very relevant topic since the appearance of the first microfluidic devices in 1990 due to the numerous advantages that these technologies can offer regarding the enhancement of techniques such as drug delivery, biological processing, computation, or encryption.<sup>1–3</sup> The main assets of this automation rely upon the small size of the systems. This leads to the use of small fluid volumes and reagents, which helps cut down costs as well as response time.<sup>2,4–6</sup> This reduction in sample volume also means that the fluid will be in the laminar flow regime. This is characterized by the fact that the sample will flow in parallel layers with no disruption between them, no crosscurrents perpendicular to the direction of the flow, and no lateral mixing or swirls will appear.<sup>4</sup> Scaling down dimensions also bears that there is a low effect produced by gravity in comparison with macroscale systems. On the other hand, phenomena such as surface tension and capillary forces become more relevant and will require special attention to theoretically describe the effects that take place.<sup>2,7,8</sup>

The medical field brings forward interesting potential applications for this kind of technology. Microfluidic lab-on-chip devices support biomedical tests that comprise many different traditionally used

analyses and techniques and can improve them in different ways. For example, they can enhance drug delivery, tests for observing pandemics, glucose monitoring, diabetic control, and diagnosis of diseases among others.<sup>5,9,10</sup>

Blood is a complex non-Newtonian fluid based on a two-phase suspension of solid elements (red blood cells [RBCs], white blood cells [WBCs], platelets, etc.) suspended in an aqueous solution of organic molecules, proteins, and salts called plasma. The apparent viscosity of blood depends on the existing shear forces (i.e., non-Newtonian behavior) and is determined by hematocrit, plasma viscosity, RBC aggregation, and the mechanical properties of RBCs. The RBCs are highly deformable, which significantly contributes to how blood flows both under bulk flow conditions and in the microcirculation.<sup>11</sup>

Alterations in the rheology of blood due to various physiopathological processes have been reported, for example, due to the alteration of hematocrit, which significantly contributes to hemorheological variations in diseases and in certain extreme physiological conditions. Also, RBC deformability is sensitive to local and general homeostasis, so RBC deformability is affected by alterations of the properties and associations of membrane skeletal proteins. This affects the ratio of

RBC membrane surface area to cell volume, cell morphology, and cytoplasmic viscosity. Such alterations may result from genetic disorders or may be induced by factors such as abnormal local tissue metabolism, oxidant stress, and activated leukocytes. Finally, RBC aggregation is mainly determined by plasma protein composition and surface properties of RBCs, with increased plasma concentrations of acute phase reactants in inflammatory disorders being a common cause of increased RBC aggregation.<sup>12</sup>

Some diseases could be diagnosed through changes that they generate in the rheological properties of blood.<sup>6</sup> Yet, at this moment, the most used technology for this kind of diagnosis is through test based on macroscale analysis of blood samples, which take long processing time and large sample quantity, and is costly.<sup>13</sup>

The addition of de-ionized water (DIW) or salts such as sodium chloride (NaCl) causes effects on the red blood cells that are similar to those presented by human pathologies; for instance, the effects related to the overhydration or dehydration (i.e., deviation of homeostasis) of the red blood cells due to a malfunction of the regulation channels and pumps in their membrane. On top of this, we also know that DIW and NaCl are used in order to achieve local homeostasis after surgeries like extensive pelvic surgery.<sup>14</sup> Therefore, it is useful to evaluate how these substances affect the red blood cell in a rheological and physiological way. This will provide medical studies with more information in order to determine which compound is best for use in different scenarios.

In this work, we will perform experiments with healthy blood that is altered with both NaCl and DIW. The final goal is the detection of diseases; hence, in this paper, we demonstrate that the device and the theoretical model are rigorous enough to depict differences due to hematocrit and tonicity alterations. With these results, in the future, we will be able to move forward into the trials with pathology-affected blood samples.

Abnormal hematocrit (ht) concentrations can also be an indication of diseases. We will perform experiments using healthy blood samples to check whether the theoretical model that has been developed and the experimental setup can distinguish the difference produced only by different concentrations of ht. On its own, this would be a huge improvement given that we could perform tests, which otherwise requires a huge amount of sample, with just the amount of blood that comes from a finger prick.

The experimental detection is based on front microrheology. This is a simple yet effective approach to measure rheological properties of a fluid flow by analyzing the dynamical behavior of the moving front. In our case, we use the change in position of the front inside a multiwidth microchannel to extract the rheological values of blood.

In our work, we study different pathologies, and we need to obtain collapsed viscosity curves. These viscosity curves will be used as the standard to which the data of the patients will have to be fitted to for determining their condition. The collapsed curves will be calculated considering the different geometries of the segments in the channel we use for the detection. With this, we can have the most general model possible as well as the widest swept range of values in a single experiment.

## II. EXPERIMENTAL SETUP

A microchannel made of polydimethylsiloxane (PDMS) is attached to the top of a glass slide, which has gold electrodes printed

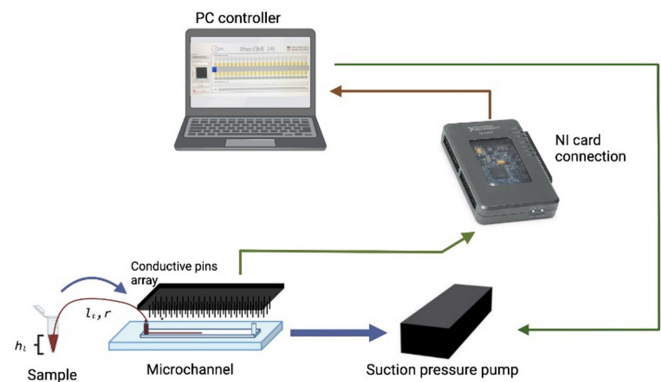


FIG. 1. Scheme of the experimental setup.

on it. The outlet of the channel is connected to a Mitos Fluika Low Vacuum Generator Pump (Part no. 3200419). When the pump is activated using the PC controller, the fluid goes into the microchannel, and the front is detected by a National Instruments card from the connection of the array of electrodes. The detection is processed by the programmed interface in the PC, Rheo Visc8, a custom-made program on LabView, which will return the time the fluid front has spent to reach each pair of electrodes in the microchannel.

The experimental configuration shown in Fig. 1 consists of a reservoir with the fluid, which is connected to the microchannel by a capillary tube.

We remark that in this specific experiment, we have used a microchannel with four different segments, which differ in terms of channel width. This is done with the purpose of getting as many data points in a single experiment as possible and then create the most accurate fit we can without needing to repeat the experiment an unnecessary number of times.

As we will see later in the model discussion, by introducing different widths in the microchannel, we will get slightly different values for the velocity and viscosity in each segment for a single value of the pressure. This will generate different fitting curves for each segment, but when we transform them into a collapsed viscosity curve, this difference will be translated to different values of shear rate. Hence, we will have a wider range of shear rates covered using a multiwidth microchannel than if we had done the same number of experiments with a single width channel. Details on the setup dimensions and the segment widths are included in Tables I and II, respectively.

When we activate the pump, the fluid gets into the microchannel entering through the widest segment, and the front is detected from the connection of an array of electrodes. When a fluid with electric conductivity, like blood, touches the two paired electrodes, they produce an electric signal. The signal is transduced by a myRIO National Instruments card and then processed by the interface developed by

TABLE I. Values of the width of the different channel segments.

	First (S_1)	Second (S_2)	Third (S_3)	Fourth (S_4)
Segments width $w_i$ ( $\mu\text{m}$ )	1000	850	700	500

TABLE II. Values of relevance of the experimental setup.

Parameter	Value
Length of the tube $l_t$ (mm)	20
Radius of the tube $r$ ( $\mu\text{m}$ )	127
Length of the segment $l_i$ (mm)	10
Height of the fluid–air interface in the reservoir $h_j$ (mm)	5
Height of the microchannel $b$ ( $\mu\text{m}$ )	290

RheoDx for this device. The computer will return the time the fluid front has spent reaching each pair of electrodes in the microchannel. Then, it automatically creates a file with the time readings for the 24 pairs of electrodes in the setup. Each mean front velocity data point is calculated from six acquired time data points from the six pairs of electrodes that are located at each segment.

In Fig. 2, we present snapshots of the fluid advancing through each one of the sections of different width of the microchannel, at a fixed pressure of 2000 Pa. The fluid advances from left to right.

As we have previously mentioned, an easy way to examine the behavior of the fluid is to study the fluid/air front advancement. In the microchannel, the front velocity ( $\dot{h}_i$ ) is defined as the change of the front position in the segment ( $\omega_i$ ), through time  $h_i(t)$ .  $h_{ij}(t)$  is defined as the average position of the front, as shown in the following equation:

$$h_i(t) = \frac{1}{N} \sum_{j=1}^N h_{ij}(t), \quad (1)$$

where  $h_i(t)$  is the average fluid-front position with respect to  $z$  axis, as shown in Fig. 3. This allows us to work with values that are independent of the position in  $z$ .

The value of the gap distance between the group of electrodes of one segment and the following is of  $8200 \mu\text{m}$  and the gap between individual electrodes in a group is  $350 \mu\text{m}$ . Hence, we can divide  $\Delta d$ , which is the separation between the electrodes, and  $\Delta t$ , which is the elapsed time,

$$\dot{h}_i(t) = \frac{\Delta d_i}{\Delta t}. \quad (2)$$

From this, we subtract the mean front velocities of the front for all the sections of the microchannel, ( $\dot{h}_{\omega_i}$ ).

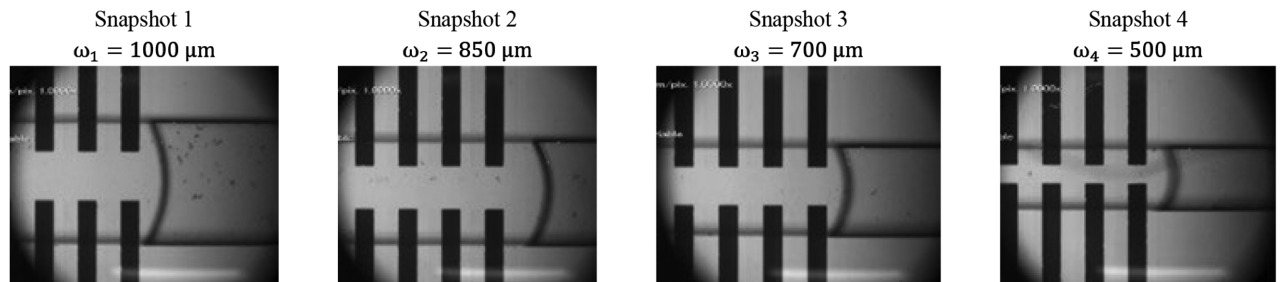


FIG. 2. Snapshots of the fluid front advancement through the four segments of the PDMS channel.

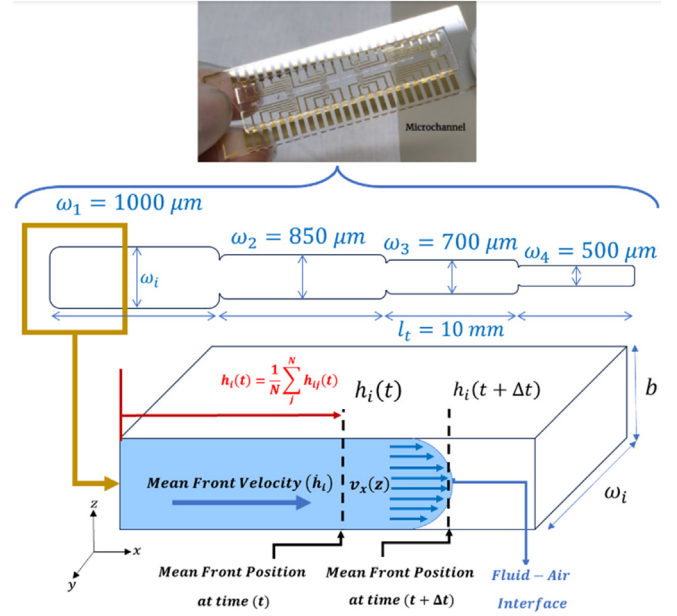


FIG. 3. Top: picture of the microchannel. Middle: representation of the microchannel where the segments with different widths can be appreciated. Bottom: representation of the fluid front advancement, where  $v_x(z)$  is the  $x$  component of velocity inside the microchannel as a function of the height ( $z$ ).  $h(t)$  is the mean front position of the fluid average in the ( $z$ ) direction.

All the values for the geometrical parameters implied in the experiment are shown in Tables I and II

### III. THEORETICAL MODEL

Our experimental system, shown in Fig. 4, is formed by three main components: a reservoir, a capillary tube, and the microchannel. Since the microchannel is divided into four segments of different widths, which will produce pressure drops as we move from one segment to the next, the pressure difference inside each region will vary.

As a result, the total pressure drop for each segment is

$$\Delta P_i = P_{\text{ipump}} + \rho g h_1 - \Delta P_t - \sum_{j=1}^{i-1} \Delta P_{R_j} - P_{\text{icap}}, \quad (3)$$

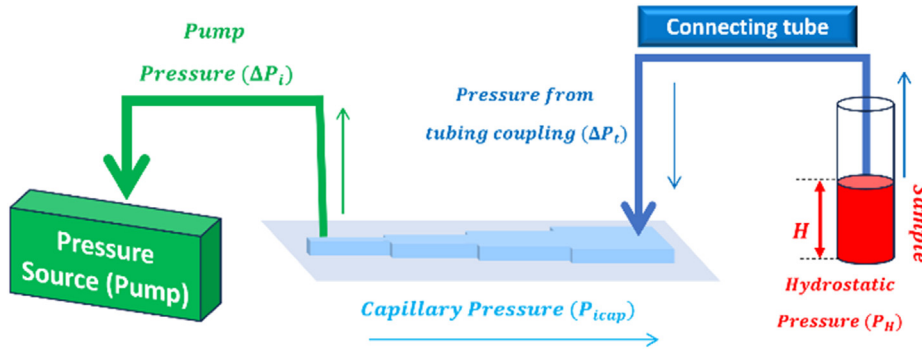


FIG. 4. Diagram of the pressures inside the experimental setup.

where  $\Delta P_i$  is the pressure drop inside the segment where we measure;  $P_{ipump}$  is the pressure exerted by the pump;  $\rho gh_i$  is the hydrostatic pressure, where  $h_i$  is the height of the fluid in the reservoir;  $\Delta P_t$  is the pressure drop inside the tube;  $\Delta P_{Rj}$  is the resistance pressure due to the filling of every segment of the microchannel before the one where we measure; and  $P_{icap}$  is the capillary pressure in the segment we measure. The pressure of the pump is the value that we set the pump to exert. The hydrostatic pressure is directly calculated by assuming that  $\rho$  is the density of the used fluid (in the case of blood at the temperature of our laboratory, it would be  $1050 \text{ kg/m}^3$ ),  $g$  is the acceleration due to gravity, and  $h_i$  is the height of the fluid in the reservoir. The other contributions to the total pressure drop are a little bit harder to calculate. The capillary pressure  $P_{icap}$  is calculated employing the Young–Laplace equation<sup>15</sup> for a rectangular channel,

$$P_{icap} = 2\tau \cos\theta_i \left( \frac{1}{b} + \frac{1}{\omega_i} \right), \quad (4)$$

where  $\tau$  is the surface tension coefficient between fluid–air, while  $b$  and  $\omega_i$  are the height and the width of the channel segment.  $\theta_i$  is the contact angle of the meniscus with the walls of the channel, calculated for each segment and exerted pressure.

The pressure drop inside the tube and inside each segment of the microchannel is calculated by means of the Stokes equation<sup>8</sup> and the flow rate definition. The shear rate is the gradient of velocities of the fluid when applying a certain stress, and it is defined as

$$\dot{\gamma}_i(z) = \frac{\partial v_x}{\partial z}. \quad (5)$$

Now, the pressure gradient can be expressed as a function of the fluid mean front position,  $h(t)$ , and the pressure drop along the system,  $\Delta P_i$ ,

$$\frac{\partial \tau_i}{\partial z} = \frac{\partial}{\partial z} [\eta \dot{\gamma}_i(z)] = \frac{\partial P_i}{\partial x}. \quad (6)$$

The shear stress  $\tau_i$  is a symmetrical tensor that when describing incompressible fluids can be expressed as follows:

$$\tau_{ij} = \eta (\partial_{xj} v_i + \partial_{xi} v_j). \quad (7)$$

By applying Eqs. (1) and (6), we obtain

$$\tau_i = \eta \dot{\gamma}_i(z) = \frac{\Delta P_i}{h_i(t)} z. \quad (8)$$

The behavior of the non-Newtonian fluids can be described as the power law model, which states that the relationship between the shear stress of the fluid when applying a certain shear strain rate is nonlinear,

$$\tau_i = m \dot{\gamma}_i^n. \quad (9)$$

Then, an equation for shear rate is obtained by using Eqs. (6) and (9),

$$\frac{\partial v_x}{\partial z} = \left( \frac{z}{m h_i(t)} \frac{\Delta P_i}{h_i(t)} \right)^{\frac{1}{n}}. \quad (10)$$

Now, we can characterize both linear and nonlinear fluids by using the Ostwald–de Waele model, also known as the power law model<sup>16–18</sup> in Eq. (11). This is a two-parameter model in which the stress at which we submit the fluid, and hence the viscosity ( $\eta_i$ ), is related to the shear rate ( $\dot{\gamma}_i$ ),

$$\eta_i(\dot{\gamma}_i) = m \cdot \dot{\gamma}_i^{n-1}. \quad (11)$$

The shear rate associated with the mean front position is defined as

$$\dot{\gamma}_i = \frac{\dot{h}_i}{b}, \quad (12)$$

where  $b$  is the smallest length of the channel we are using, and the sub-indexes ( $i$ ) refer to the segment of the microchannel we are evaluating.

From Eq. (11), it is seen that the viscosity of a non-Newtonian fluid depends on the shear rate as well as on the ( $n=1$ ) exponent. This shear rate has no dependence in  $z$ .  $n$  is a characteristic parameter of the model that allows for the fluid to be characterized in different categories depending on the value it takes. If  $n > 1$ , we have shear thickening behavior, and there is an increase in the viscosity as we increase the shear rate. If  $n < 1$ , we have shear thinning behavior, and as shear rate increases, there is a descent in viscosity. In the case  $n = 1$ , we recover the characteristic linear expression for a Newtonian fluid.  $m$  is a parameter that also characterizes the nature of the fluid, and if it is Newtonian, it will be equal to the viscosity of the fluid. For a non-Newtonian fluid, when the  $\dot{\gamma} = 1$ ,  $m$  will be the viscosity at that specific value of the shear rate,

$$\Delta P_i(t) = \frac{2m}{b} h_i(t) \dot{h}_i(t)^n \left[ \frac{2}{b} \left( \frac{1}{n} + 2 \right) \right]^n. \quad (13)$$

Considering that the microchannel and the tubing are two coupled sections, they comply with the mass conservation principle, and



we know that the flow inside the channel section,  $Q_i$ , depends on front velocity,

$$Q_i = \dot{h}_i \omega_i b, \quad (14)$$

where the segment width at each section is  $\omega_i$ , and the channel height is  $b$ . Now, the shear rate in segment  $\omega_i$  is  $(\dot{\gamma}_i = \frac{\dot{h}_i}{b})$ . From previous articles,<sup>17</sup> we have determined that the term  $\Delta P_i$  can be written as the product of the hydraulic resistance inside the microchannel,  $S_i$ , that is dependent on  $m$ ,  $n$ , and the geometric parameters of the channel segment. Therefore,  $\Delta P_i$  is

$$\Delta P_i = S_i Q_i^n = m \dot{h}_i(t) \left( \frac{2}{b} \right)^{(1+2n)} \left( \frac{1}{n} + 2 \right)^n Q_i^n. \quad (15)$$

Knowing that the flow depends on front velocity ( $Q_i = \dot{h}_i \omega_i b$ ), we can now express the pressure inside the channel at each segment,  $\Delta P_i$ , as

$$\Delta P_i = m \dot{h}_i(t) \left( \frac{2}{b} \right)^{1+n} \left( \frac{1}{n} + 2 \right)^n \dot{h}_i^n. \quad (16)$$

Now, the pressure drop inside the tubing,  $\Delta P_t$ , can be expressed as the product of  $S_t$  and  $Q_t^n$ . Where  $S_t$  is the hydraulic resistance of the tubing, which depends on  $m$ ,  $n$ , and the tubing parameters  $r$ ,  $l_t$ . The flow inside the tubing is  $Q_t$ ,

$$\Delta P_t = S_t Q_t^n = m 2l_t \left( \frac{1}{\pi r^2} \right)^n \left( \frac{1}{r^{1+n}} \right) \left( \frac{1}{n} + 3 \right)^n Q_t^n. \quad (17)$$

Considering the flow dependence on flow velocity inside the tubing ( $Q_t = \pi r^2 v_t$ ) and the mass conservation inside the coupled system, the relation  $Q = Q_t \rightarrow \omega_i b \dot{h} = \pi r^2 v_t$  for the coupled system in this study,  $\Delta P_t$ , can be written as follows:

$$\Delta P_t = m 2l_t \left( \frac{\omega_i b}{\pi r^2} \right)^n \left( \frac{1}{r^{1+n}} \right) \left( \frac{1}{n} + 3 \right)^n \dot{h}_i^n, \quad (18)$$

$$\Delta P_i(t) = \frac{2m}{b} \dot{h}_i(t) \dot{h}_i(t)^n \left[ \frac{2}{b} \left( \frac{1}{n} + 2 \right) \right]^n, \quad (19)$$

and

$$\Delta P_t = \frac{2l_t m \left( \frac{1}{n} + 3 \right)^n}{r^{1+n}} v_t^n. \quad (20)$$

The resistance pressure will have the same expression but because it is due to the segment being filled,  $\dot{h}_i(t)$  and  $\dot{h}_i(t)$  are replaced by the length of the segment,  $l_i$ , and the mean front velocity in it,  $\dot{h}_i$ ,

$$\Delta P_{R_j} = \frac{2m}{b_j} l_j \dot{h}_j^n \left[ \frac{2}{b_j} \left( \frac{1}{n} + 2 \right) \right]^n. \quad (21)$$

The calculations can be found in the bibliography.<sup>18–20</sup>

Now that we have all the contributions calculated, we will substitute for each segment using Eq. (3). Using the principle of mass conservation,

$$v_t \pi r^2 = \dot{h}_i \omega_i b_i \forall i \quad (22)$$

and grouping the terms that are not velocity dependent in a term, which we will call effective pressure, we rewrite a general expression,

$$P_{\text{eff}} = P_{\text{pump}} + \rho g h_l - P_{\text{icap}}. \quad (23)$$

From previous results,<sup>19</sup> we know that in the existing conditions of our experimental setup and for all  $t$ , the resistance associated with the fluid flow inside the segment, which we calculate, is much smaller than the ones associated with the tube and the previous segments,

$$\Delta P_{\text{eff}}(t) \ll \Delta P_t + \sum_{j=1}^{i-1} \Delta P_{R_j}. \quad (24)$$

These conditions allow us to have time-independent velocity,  $\dot{h} / = \dot{h}(t)$ , and the general expression ends up with this aspect,

$$P_{\text{eff}} = K_i(m, n) \dot{h}_i^n. \quad (25)$$

The pressure inside the couple system can be written as

$$P_{\text{eff}} = P_{\text{ipump}} + P_H - P_{\text{icap}} = \Delta P_t + \Delta P_i \\ = m \left[ 2l_t \left( \frac{\omega_i b}{\pi r^2} \right)^n \left( \frac{1}{r^{1+n}} \right) \left( \frac{1}{n} + 3 \right)^n + h(t) \left( \frac{2}{b} \right)^{1+n} \left( \frac{1}{n} + 2 \right)^n \right] \dot{h}_i^n, \quad (26)$$

$$K_i(m, n) = m \left[ \frac{2l_t \left( \frac{1}{n} + 3 \right)^n}{r^{1+n}} \left( \frac{b_i \omega_i}{\pi r^2} \right)^n + \sum_{j=1}^{i-1} \frac{l_j \left( \frac{1}{n} + 2 \right)^n}{\left( \frac{b_j}{2} \right)^{1+n}} \left( \frac{\omega_j b_i}{\omega_j b_j} \right)^n \right], \quad (27)$$

where  $n$  and  $m$  are dependent of the fluid we analyze, and the rest of the terms are geometrical parameters of the system (Table I). When  $n \neq 1$ , these equations will allow us to characterize non-Newtonian fluids, and with  $n = 1$ , we will recover a model for the Newtonian ones.

#### IV. EXPERIMENTAL METHOD

To determine whether a fluid is Newtonian or non-Newtonian, we can use a two-parameter power law expression,

$$\sum P_i = A_i \dot{h}_i^n, \quad (28)$$

where  $\sum P_i$  is the sum of pressure contributions that are not velocity dependent in the evaluated segment; hence,  $\sum P_i = P_{\text{eff}}$ .  $\dot{h}_i$  is the velocity of the fluid front in the segment, and finally,  $n$  and  $m$  are characterizing fluid constants. These types of equations are comparable to the ones found with the theoretical model Eq. (25). The data that we collect from the experiments are the velocities or each applied pressure. With these, we can find equations like Eq. (28), with which we can define the fluids nature.

It would seem like we can control every variable in the  $P_{\text{eff}}$  but there are factors like fluctuation of the pressure injected by the pump, changes in the contact angle, and/or others that may be significant and which we cannot quantify exactly. Regarding these possible effects, the following procedure was implemented:

First, graph and show equations for the pressure of the pump in front of the velocity but leaving a free parameter

$$P_{\text{pump}} = A_i' h_i^{n'} + B_i', \quad (29)$$

$$P_{\text{expi}} = P_{\text{pump}} - B_i' = A_i' h_i^n. \quad (30)$$

$B_i'$  is the rest of the contributions that should be found in the effective pressure. We have experimentally checked that the residual pressure,  $B_i$ , is given by the  $P_H$  and  $P_{\text{icap}}$  in Eq. (26). The next step is to subtract this  $B_i'$  contribution to the pump pressure and then recalculate the equation.

If we now take logarithms on both sides of Eq. (30), we get

$$\log(P_{\text{expi}}) = \log(A_i) + n \log(h_i). \quad (31)$$

The slope of Eq. (31) is  $n$ . If we now compare Eq. (30) to Equation (25), we can recognize that

$$A_i = K_i(m_i, n). \quad (32)$$

Isolating  $m_i$  from Eq. (30), we get

$$m_i = \frac{A_i}{\left[ \frac{2l_t \left( \frac{1}{n} + 3 \right)^n}{r^{1+n}} \left( \frac{b_i \omega_i}{\pi r^2} \right)^n + \sum_{j=1}^{i-1} \frac{l_j \left( \frac{1}{n} + 2 \right)^n}{\left( \frac{b_j}{2} \right)^{1+n}} \left( \frac{\omega_j b_i}{\omega_j b_j} \right)^n \right]}. \quad (33)$$

Using Eq. (32), we can rewrite Eq. (2) for non-Newtonian fluids, and this substitution gives us

$$\eta_i(\dot{\gamma}_i) = \left( \frac{A_i}{\frac{2l_t \left( \frac{1}{n} + 3 \right)^n}{r^{1+n}} \left( \frac{b_i \omega_i}{\pi r^2} \right)^n + \sum_{j=1}^{i-1} \frac{l_j \left( \frac{1}{n} + 2 \right)^n}{\left( \frac{b_j}{2} \right)^{1+n}} \left( \frac{\omega_j b_i}{\omega_j b_j} \right)^n} \right) \dot{\gamma}_i^{n-1}. \quad (34)$$

This is a general expression that gives us the viscosity of a fluid as a function of the shear rate it experiences. The viscosity of a fluid depends mostly on the geometrical parameters of the system as well as the characteristic  $n$  value. As for Newtonian fluids, we know that  $\eta = m_i$ , so their general viscosity expression will be just Eq. (33), but by substituting  $n = 1$ ,

$$\eta_i = \frac{A_i}{\frac{8l_t}{r^2} \left( \frac{b_i \omega_i}{\pi r^2} \right) + \sum_{j=1}^{i-1} \frac{12l_j}{b_j^2} \left( \frac{\omega_j b_i}{\omega_j b_j} \right)}. \quad (35)$$

We will fit the corresponding data to Eqs. (29) and (33) if it is non-Newtonian or to Eq. (35) if it is Newtonian.

## V. EXPERIMENTAL RESULTS

We have conducted two separate sets of experiments that have two very different aims. The first set is an experiment done with healthy blood and plasma. These are done to validate that our device and theoretical model differentiate between samples with different red blood cell percentage, hence different hematocrit. The second set of experiments is done with altered blood using NaCl and DIW to see the effect these have in erythrocytes and in the rheological properties of the samples. We have taken images of our samples using an optical microscope with a fast CCD (charge-coupled device) camera attached to it to determine whether there is any visual alteration of the red blood cells due to the manipulation and alteration. The blood has been proportioned by the Banc de Sang I Teixits (BST) from anonymous healthy donors. The use of these samples was authorized by the Bioethics Committee of the University of Barcelona (IRB 00003099). Due to this, when we receive sample tubes, we know we are working with healthy blood, but we do not know the hematocrit concentration of the specimen. To characterize the different hematocrit levels, we prepared samples with the desired RBC concentration. This is done by first centrifuging the whole blood. Then, we separated it into three phases: top fluid being plasma; then a thin layer of buffy coat, which contains between others the leukocytes and platelets; and, below these, the erythrocytes. With the help of a pipette, we separate the plasma plus buffy coat and the erythrocytes in different containers. Now, we can prepare the percentage of hematocrit we want just by knowing the final volume we want our sample to have.

### A. Hematocrit differentiation experiments

We conducted experiments with known prepared hematocrit concentrations to study the difference that this generates in the rheological properties of the blood sample. The experiments were conducted using the same whole blood sample on the same day. We prepared samples of 40% and 30% ht concentration as well as one that was just plasma. Plasma is used to compare blood samples to a well-characterized fluid.

Figure 5 presents an image taken with the CCD camera of the red blood cells in the prepared samples. After the hematocrit

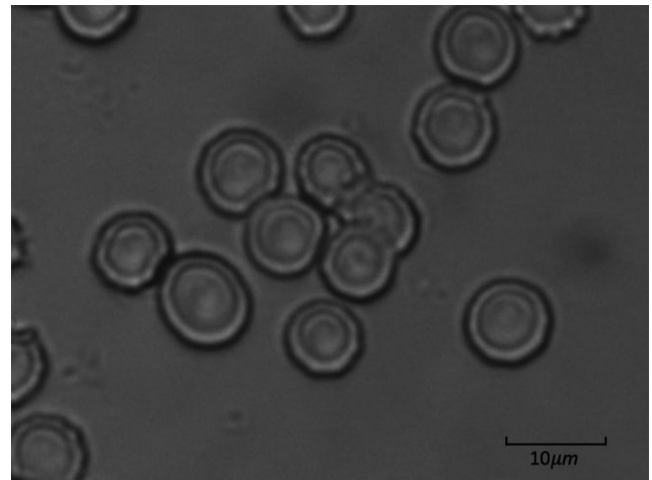


FIG. 5. Optical microscope image of healthy red blood cells.

**TABLE III.** Values of the  $n$  exponent of blood with different hematocrit concentrations at the different channel segments.

Sample	$n_{s_1}$	$n_{s_2}$	$n_{s_3}$	$n_{s_4}$
40% ht	0.809	0.802	0.801	0.806
30% ht	0.842	0.847	0.843	0.851
Plasma	0.998	0.992	0.995	1.001

preparation, the erythrocytes appear without any alteration due to our manipulation.

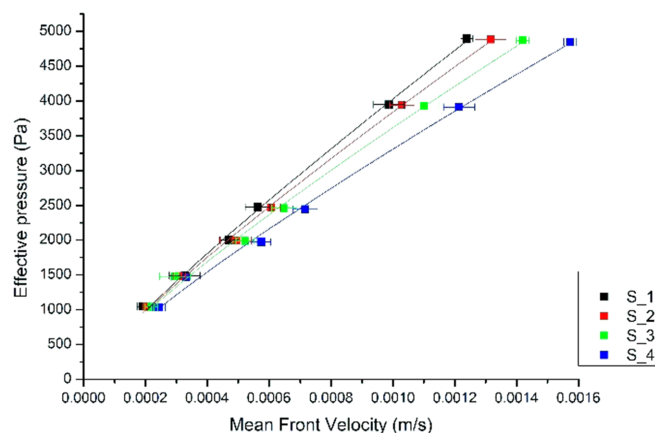
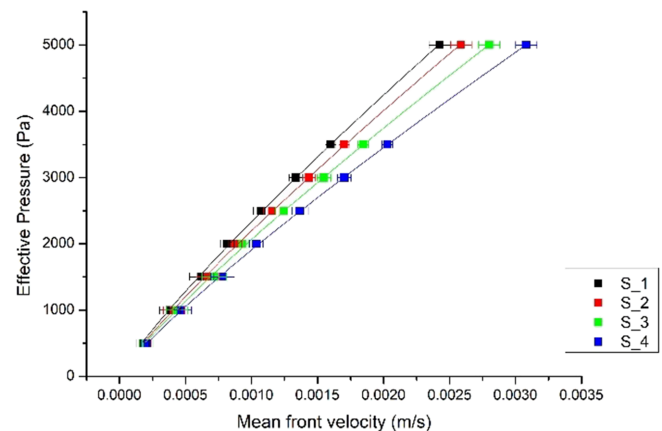
Now that we have visual proof of the good state of our samples, we run them through the experimental setup and characterize them by applying the theoretical model described. This will fit the data to Eqs. (30) and (34) to get the values of  $n$  and the viscosity curves. After this is done, we obtain Table III and Figs. 6–13. Later, in Sec. VB, we will obtain the equations for collapsed viscosity curves.

In Figs. 6 and 7, we find the curves of the effective pressure in front of the mean front velocity for blood [Eq. (30)] at 40% and 30% ht concentrations, respectively. Here, we use linear interpolation segments between measured data points to show the trend. We see that for the different segments, we get different slopes, and this is due to the different geometries of the segments. The fact that the steepest curve corresponds to the widest segment and the mildest to the narrowest one is in accordance with the mass conservation principle.

The  $n$  exponent remains constant for each sample when experimental error is considered, independently to the segment, where it is measured (Table III).

Evaluating the exponents in Table III, we see that the sample with 30% ht has  $n$  closer to 1 than the sample with 40% ht. Recalling the meaning of the exponent  $n$ , these values are telling us that the sample with 30% ht is more Newtonian than the 40% ht one. It is in accordance with the theory, as the former one contains more plasma than the latter.

In Figs. 8 and 9, we find the curves of the viscosity [Eq. (34)] in front of the shear rate. In both cases, the values of the different segments differ due to the different geometries. The segment with the

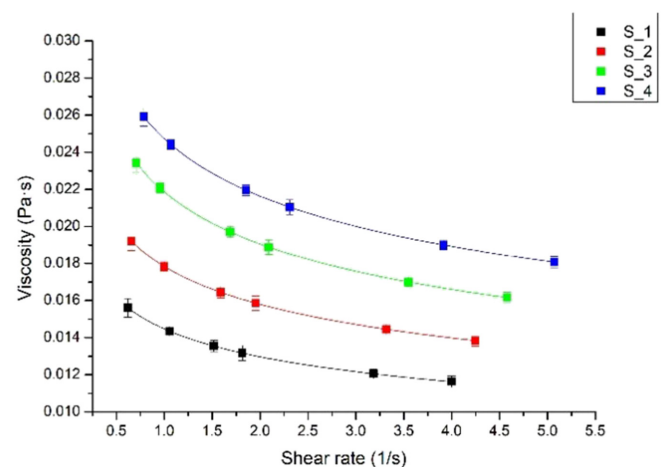
**FIG. 6.** Effective pressure as a function of velocity for blood at 40% ht in different segments (Table I).**FIG. 7.** Effective pressure as a function of velocity for blood at 30% ht in different segments.

higher values of the viscosity corresponds to the narrowest segment and the lower values to the widest one. This is due to the narrowest segment, the RBC being more packed and hence the fluid advancing with more difficulty—more viscosity. The contrary will happen for the widest one, and this is what we see reflected in our results.

Another remarkable observation is that as we go to higher values of the shear rate, the curves start to flatten. This means that at high enough values of the shear rate, blood at these hematocrit concentrations starts to behave as a Newtonian fluid.

## B. Collapsed viscosity curve calculation

These viscosities are geometry-dependent, but we are interested in a general magnitude that would only depend on the rheological properties of the fluid. This is important because the collapsed viscosity curve obtained will be used as the standard to which we will compare the patients' data without the contribution of the geometric parameters of the setup. Another advantage of the conversion to the

**FIG. 8.** Viscosity as a function of the shear rate ( $\dot{\gamma}_i/\dot{\gamma}_1$ ) of blood at 40% ht in different segments (Table I).



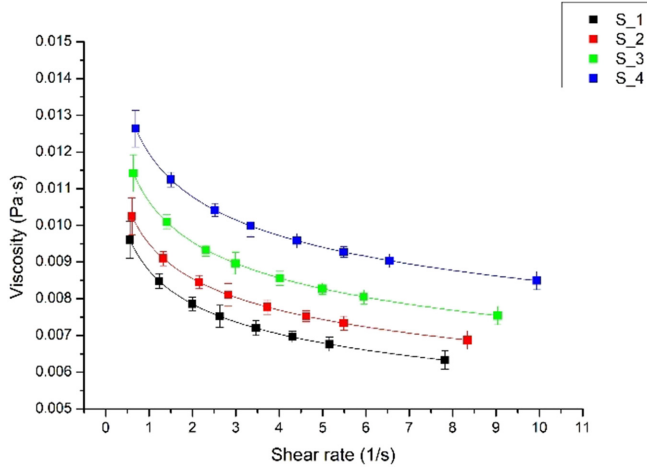


**FIG. 9.** Viscosity as a function of the shear rate ( $\dot{\gamma}_i$ ) of blood at 30% ht in different segments.

collapsed viscosity curve is that the different widths of the segments will translate to a broader range of shear rates swept in the same number of experiments as when doing those using a single width channel.

To forge this collapsed viscosity curve, we need to impose the viscosities to be the same in all segments and use one as the viscosity curve to which we want the others to collapse to. The choice of curve is arbitrary; in our case, we established that

$$\bar{\eta}_i = \eta_1. \quad (36)$$

Recalling Eq. (3), we get

$$m_i \cdot \dot{\gamma}_i^{n-1} = m_1 \cdot \dot{\gamma}_1^{n-1}. \quad (37)$$

If we isolate  $\dot{\gamma}_1$ , we get

$$\dot{\gamma}_1 = \left( \frac{m_i}{m_1} \right)^{1/(n-1)} \cdot \dot{\gamma}_i = \bar{\dot{\gamma}}, \quad (38)$$

where we have named  $\bar{\dot{\gamma}}$  the effective shear rate that would satisfy the condition of equal viscosities for each segment.

Hence, for the viscosities to collapse, we would be multiplying their slope by a constant that satisfies  $m_i = C_i \cdot m_1$ , where  $C_i$  is a dimensional constant.

If we use this equivalence and rewrite Eq. (22), we have

$$\bar{\dot{\gamma}} \bar{\eta} = \left( \frac{1}{C_i} \right)^{1/(n-1)} \cdot \dot{\gamma}_i \left( \frac{1}{C_i} \right)^{1/(n-1)} \cdot \dot{\gamma}_i. \quad (39)$$

Now, we have our collapse relation, which can be applied as a simple multiplication of a constant to the shear rate.

This constant can be calculated theoretically by recalling that  $C_i = \frac{m_i}{m_1} C_i = \frac{m_i}{m_1}$  and Eq. (33), which leads to

$$C_i = \frac{A_1}{A_i} \cdot \left[ \frac{2l_t \left( \frac{1}{n} + 3 \right)^n + \sum_{j=1}^{i-1} l_j \left( \frac{1}{n} + 2 \right)^n \left( \frac{\omega_j b_j}{\omega_i b_i} \right)^n}{\frac{2l_t \left( \frac{1}{n} + 3 \right)^n}{r^{1+n}} \left( \frac{b_i \omega_i}{\pi r^2} \right)^n} \right]. \quad (40)$$

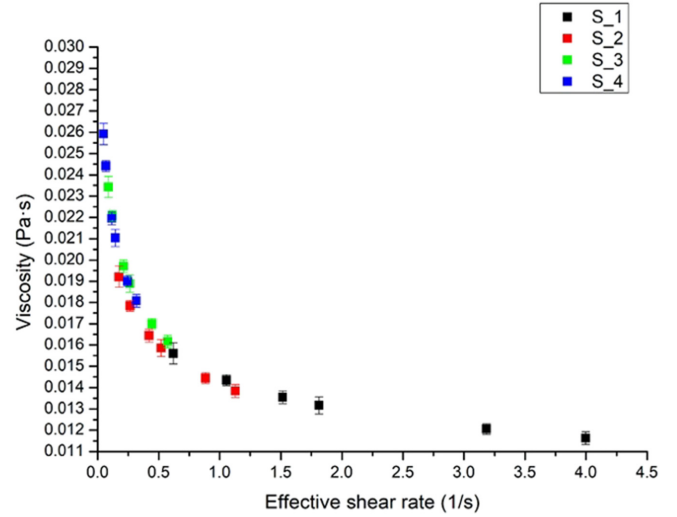


**FIG. 10.** Viscosity as a function of the effective shear rate ( $\dot{\gamma}_i$ ) for blood at 40% ht in different segments.

Equation (40) gives us the collapsed viscosity for any biocomplex fluid.

In Figs. 10–12, we have applied Eq. (40) to obtain the viscosity as a function of the effective shear rate, the collapsed viscosity curves for both samples. A similar procedure can be performed to collapse the curves for the effective pressure vs mean front velocity.

Finally, in Fig. 12, we have represented the collapsed viscosity curves for the 40% ht, 30% ht, and plasma samples. With this comparison, we can see that the viscosity of the sample at 40% ht is the one with the highest values, followed by the sample at 30% ht and the plasma one. It is the presence of erythrocytes that gives blood a different behavior from an aqueous solution, as plasma is a Newtonian fluid. The higher the RBC concentration of the sample, the more viscous and less Newtonian it will be.

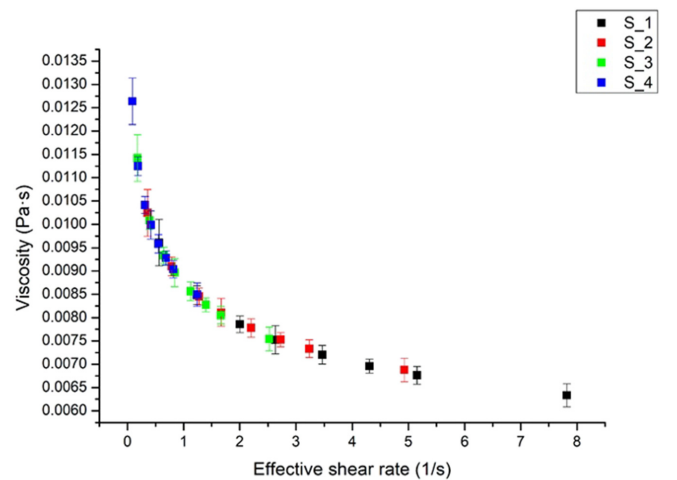


**FIG. 11.** Viscosity as a function of the effective shear rate ( $\dot{\gamma}_i$ ) for blood at 30% ht in different segments.

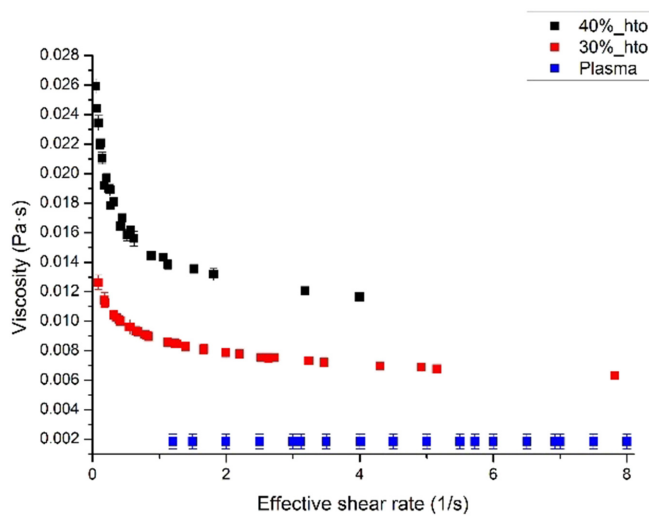


FIG. 12. Viscosity as a function of the effective shear rate ( $\dot{\gamma}_i \dot{\gamma}_i$ ) for blood at 40% ht, blood at 30% ht, and plasma.

Now, we represent Figs. 10–12 in log–log scale in Figs. 13–15, respectively. By representing these curves in log–log scale, we can see that our experimental data show power law behavior.

### C. Altered blood experiments

It is well known that red blood cell deformability is critical for optimal rheology.<sup>21</sup> These optimal conditions are reached when the volume of each human red blood cell is kept at what is known as the optimal-volume-ratio range (OVR) a fraction of about 0.55–0.60 of the maximal spherical volume allowed by its membrane area. This is because the discocyte shape allows RBCs to deform, fold, and squeeze against the walls of capillaries, exposing maximal surface area thus offering minimal diffusional distances for rapid  $O_2$  and  $CO_2$  exchanges

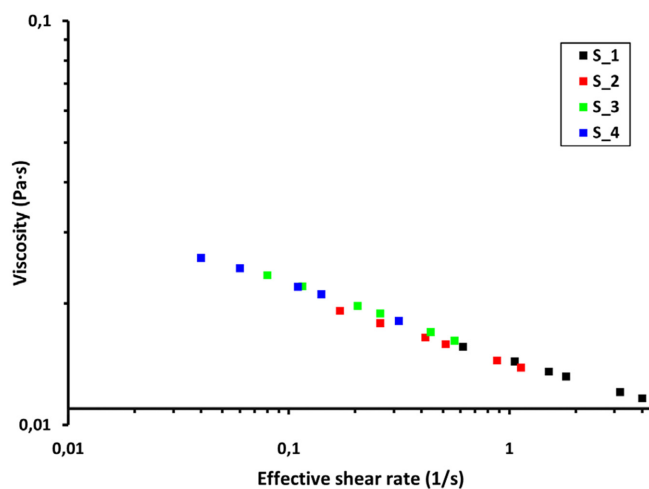


FIG. 13. Viscosity as a function of the effective shear rate ( $\dot{\gamma}_i \dot{\gamma}_i$ ) for blood at 40% ht in different segments in log–log scale.

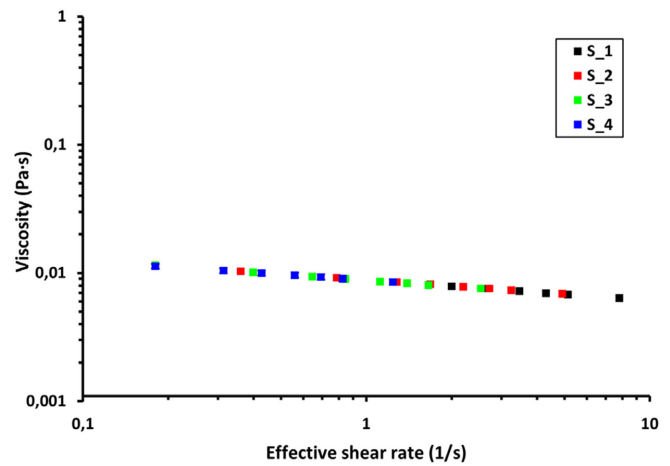


FIG. 14. Viscosity as a function of the effective shear rate ( $\dot{\gamma}_i \dot{\gamma}_i$ ) for blood at 30% ht in different segments in log–log scale.

across the capillary walls. Thus, the maintenance of the discocyte shape is essential for preserving the optimal viability and functional capacity of the cells for an extended circulatory lifespan.<sup>22</sup> These results are consistent with the literature.<sup>16,17</sup>

With OVR values above 65% (swelling) and below 50% (dehydration), cell deformability and rheology become compromised, though by different mechanisms at each end. This volume control in mature RBCs is entirely dependent on the combined function of a set of active and passive native membrane transporters. Even though they ensure cell stability under normal conditions, in inherited hematological disorders, such as sickle cell disease, thalassemia, hereditary xerocytosis, or malaria, these transporters are altered causing some serious issues.<sup>23–25</sup>

The most relevant passive and active membrane transporters whose abnormal activity would lead to these diseases are the PIEZO1 channel, the Gardos channel,<sup>21</sup> and the sodium–potassium pump.

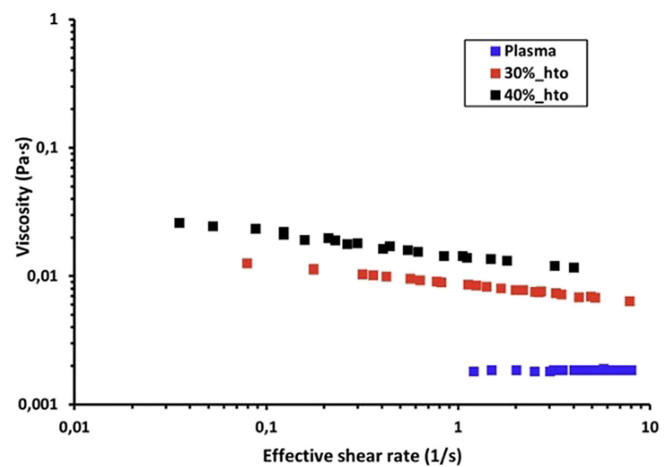


FIG. 15. Viscosity as a function of the effective shear rate ( $\dot{\gamma}_i \dot{\gamma}_i$ ) for blood at 40% ht, blood at 30% ht, and plasma in log–log scale.

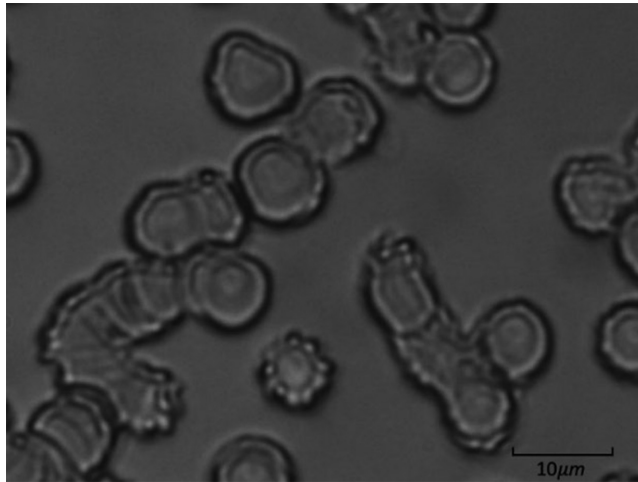


FIG. 16. Optical microscope image of hemolyzed RBC due to DIW addition.

TABLE IV. Values of the  $n$  exponent of blood with 40% RBC in just plasma in de-ionized water or sodium chloride.

Sample	$n_{s_1}$	$n_{s_2}$	$n_{s_3}$	$n_{s_4}$
40% RBC with DIW	0.809	0.802	0.801	0.806
40% ht	0.842	0.847	0.843	0.851
40% RBC with DIW	0.998	0.992	0.995	1.001

These ion influx and efflux regulators work by different means that can be found in the literature.<sup>21</sup> This could be explained as a matter of the cells being overhydrated or dehydrated, leading, respectively, to hemolysis or crenation of the erythrocytes. By altering healthy blood samples with either DIW or NaCl, we can create osmotic pressure differences.<sup>26</sup> This will make the RBC overhydrated or dehydrated, and we can recreate the effects these different diseases have on the rheology

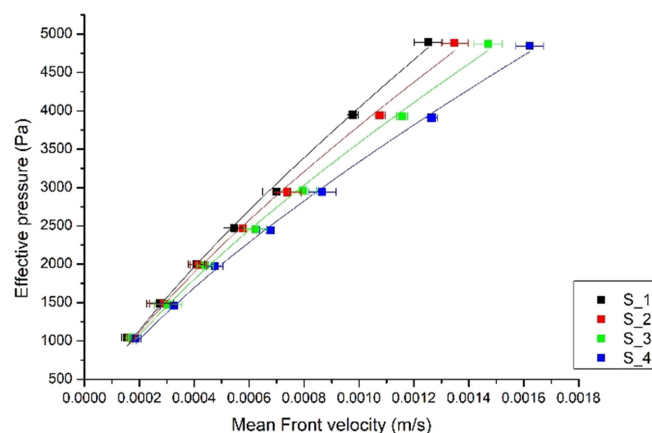


FIG. 17. Effective pressure as a function of the velocity of blood altered with DIW in different segments (Table I).

of the blood under study. Here, we evaluate altered blood samples that emulate the forenamed type of abnormalities in red blood cells, using our device and theoretical model.

The prepared dissolutions contain 40% erythrocytes, 35% plasma, and 25% of DIW in one case and NaCl in the other. This is done to have the same theoretical hematocrit concentration as the 40% ht sample we have previously evaluated, making simple the comparison between them. Part of the sample will be used to take images to compare the visual differences of the normal erythrocytes and the ones that have gone under alterations due to osmotic gradients (Figs. 5, 16, and 19).

### 1. Deionized water

When red blood cells are inserted in distilled water, there will be an influx of water, given the hypotonic character of the external medium.<sup>27</sup> Hence, the red blood cell will gain water and swell. If the intake is large enough, the integrity of their membranes is disrupted, allowing for the escape of their hemoglobin, which dissolves in the external medium. This is known as hemolysis.

Figure 16 is an image taken of the red blood cells in the prepared samples that have been altered with de-ionized water. Compared with Fig. 5, we can see that there has been a clear change in the shape of the RBC. Some appear bigger than those in the unaltered sample, while others simply look like they are just an empty, deflated membrane.

We noticed an increase in hematocrit. This increase leads to a higher viscosity in reference to the unaltered sample as it has been seen in Fig. 14.

In Fig. 18, we find the curves of the viscosity in front of the shear rate. They have an analogous non-Newtonian behavior to that of the unaltered sample.

Following the same procedure as the one seen in Subsection V A, we run the samples through the experimental setup and apply the theoretical model equations. We obtain the values on the first row of Table IV and Figs. 17 and 18.

Analyzing the results, we find the regressions of the effective pressure in front of the mean front velocity (Fig. 17). The overall behavior

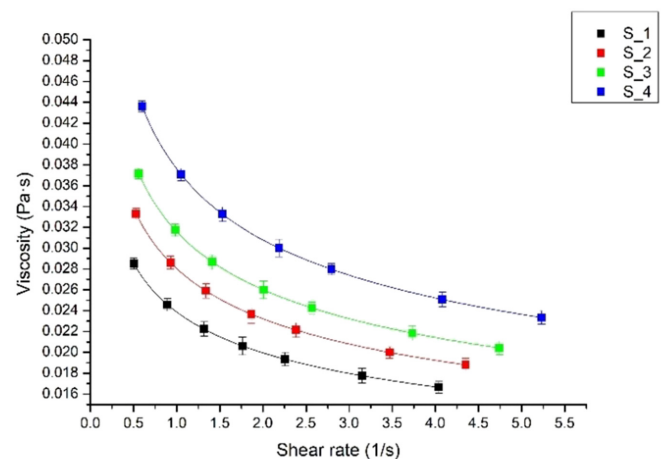


FIG. 18. Viscosity as a function of the shear rate of blood altered with DIW in different segments.

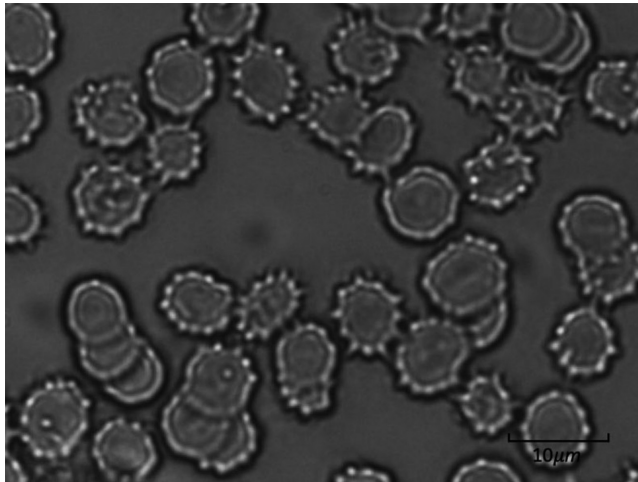


FIG. 19. Optical microscope image of crenated RBC due to NaCl addition.

is very analogous to that observed for the healthy sample (Fig. 7), but when we look at the values of  $n$  (Table IV), we see that they are all well below the unaltered blood sample value. We see that DIW causes blood to have an even more non-Newtonian behavior. This is in accordance with the cell changes that we see in Fig. 16. In other experiments,<sup>15</sup> it is shown that the addition of DIW will produce complete hemolysis. Since we only wanted to cause partial hemolysis, we used a solution of 40  $\mu\text{l}$  of erythrocytes and 35  $\mu\text{l}$  of plasma and added only 25  $\mu\text{l}$  of DIW. Given that we have used a small amount of DIW, there only has been partial hemolysis, which means that we have not completely destroyed erythrocytes; thus, some with their membrane is still intact but with a very high OVR due to the DIW intake.

Therefore, a small proportion of hemolysis is observed, which increased hemoglobin in the plasma compared with the unaltered blood. The remaining cells that had not been lysed have increased in size, causing the same effect as if we had an increase of hematocrit. This increase leads to a higher viscosity in reference to the unaltered sample as it has been seen in Fig. 12.

## 2. Sodium chloride

When subjected to hypertonic media, erythrocytes lose their normal biconcave shape, undergoing collapse and shrink unevenly due to the rapid osmotic efflux of water forming spikes. This shrinking is termed crenation or plasmolysis.

It is well known that erythrocytes are isotonic with NaCl solutions of 154 mM (0.9 wt. %/vol. %).<sup>14,28,29</sup> To reproduce realistic conditions when compared to pathological environments, we do not want very extreme acidification of the media in which the RBCs are found. Hence, we will be using a NaCl solution with a molarity of 166 mM (0.6 wt. %/vol. %), which will be just enough to create a hypertonic surrounding.

Figure 19 is an image taken of the red blood cells in the prepared samples that have been altered with de-ionized water. Compared with Figs. 5 and 16, we see another clear change in the shape of the RBC. These have little spikes in the membrane, as well as a noticeable

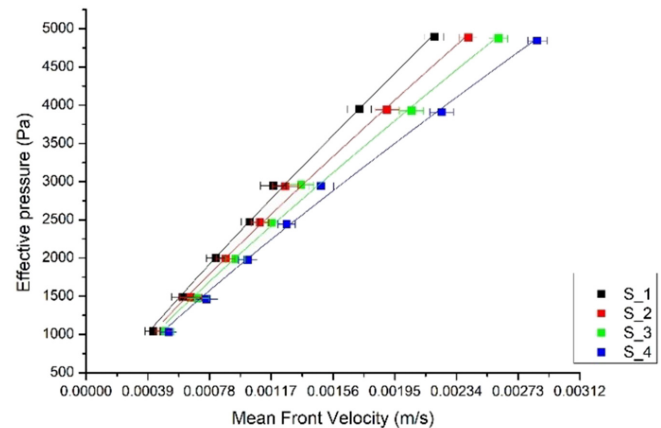


FIG. 20. Effective pressure as a function of velocity of blood altered with NaCl in different segments (Table I).

reduction of their overall size. With this optical verification, we can also confirm the hypotonic character of our solution.

Following the same procedure as in Subsections V A and V C 1, we run the samples through the experimental setup and the model equations. We obtain the values on the third row of Table IV and Figs. 20 and 21.

Analyzing our data and taking the regressions of the effective pressure in front of the mean front velocity (Fig. 20), we see that the overall behavior is akin to the observed for the healthy and DIW samples<sup>27</sup> (Figs. 6 and 16). However, when we look at the values of  $n$  (Table IV), we observe that they are all well above the other sample values. Hence, we see that NaCl causes blood to have a more Newtonian behavior. These results are coherent with the theoretical knowledge and previous experiments.<sup>17,21,25</sup> Red blood cells in a hypertonic solution crenate, leading to a decrease in the hematocrit of the solution in comparison with that of the non-hemolyzed blood of the unaltered sample. This is because the cells take up less space due to

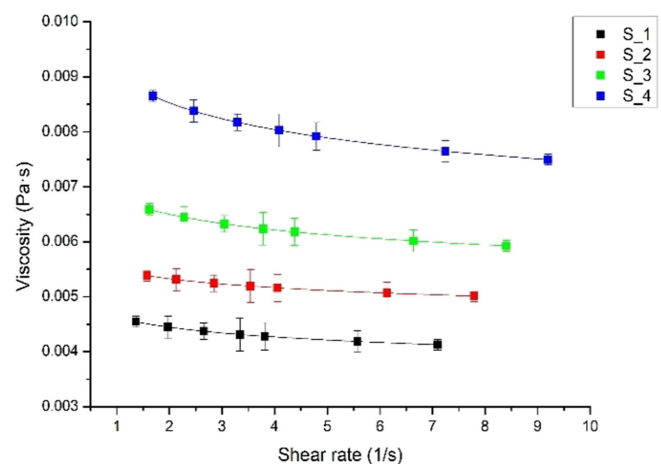
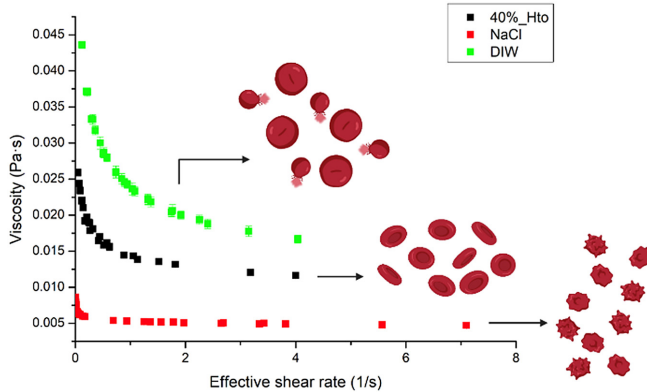


FIG. 21. Viscosity as a function of the shear rate of blood altered with NaCl in different segments.





**FIG. 22.** Viscosity as a function of the effective shear rate of blood altered with NaCl, blood altered with DIW, and blood at 40% ht in log–log scale.

the rapid loss of water, which in turn will create a more aqueous-like, less viscous solution.

In Fig. 21, we find the curves of the viscosity of the fluid in each segment in front of the shear rate. We have an overall analogous behavior to that one for the unaltered sample. However, we can see that the change of the viscosity as the shear rate is modified is far smaller than in the other previous two cases. This is another sign of the more Newtonian nature of the sample.

In Sec. IV, we present Fig. 22 for the collapse of healthy blood at 40% ht and altered with DIW and NaCl.

## VI. DISCUSSION AND CONCLUSIONS

In Fig. 22, we have represented the collapsed viscosity curves for the 40% ht, DIW altered, and NaCl altered samples to compare the viscosities between them. We can see that the viscosity of the DIW altered sample is the one with the highest values, followed by the sample at 40% ht, and finally, the NaCl altered one. We know that the addition of DIW provokes a hematocrit increase and that of NaCl, a hematocrit decrease with respect to the non-altered, same initial erythrocyte concentration one.<sup>29</sup>

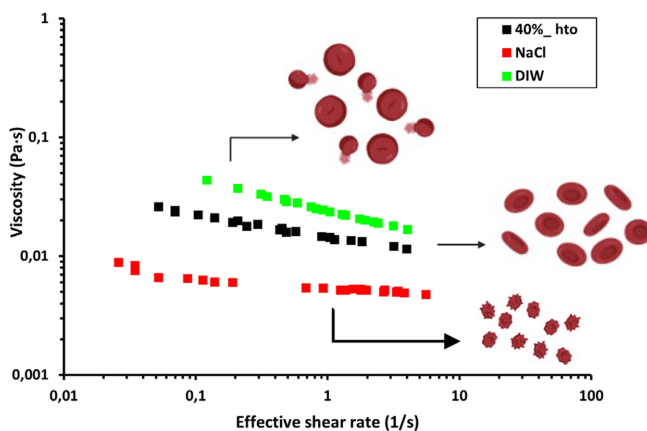


**FIG. 23.** Viscosity as a function of the effective shear rate of blood altered with NaCl, blood altered with DIW, and blood at 40% ht.

When we alter the samples with DIW and NaCl, we are changing the initial theoretical RCB concentration. Therefore, it is like changing the apparent hematocrit in an unaltered sample. Thus, we can compare the conduct in Fig. 22 with the behavior of different unaltered hematocrit samples (Fig. 12) we see an analogous effect; the highest values of viscosity correspond to the highest apparent hematocrit. This is because it is the presence of erythrocytes what makes the blood different from an aqueous solution; hence, the higher the concentration of RBCs, the more viscous the sample will be.

In Fig. 23, we add Fig. 22 in log–log to see the power-law behavior of the results.

We present a theoretical model that describes both the behavior of Newtonian and non-Newtonian fluids inside a multiwidth micro-channel to extract collapsed viscosity curves. This will allow us to compare between samples over a wider range of values as well as a standard that will be used to relate patients' data to different rheologically distinct pathologies. Experiments using samples of blood with different hematocrit concentration as well as differently altered blood were carried out.

From the experiments with different hematocrit concentrations, it was seen that the sample with 30% ht has  $n$  closer to 1 than the sample with 40% ht (Table III), meaning that the sample with 30% ht is more Newtonian than the 40% ht one, which is following the theory, as the former one contains more plasma than the latter. When we represented the collapsed viscosity curves for them (Fig. 12), it was seen that the viscosity of the sample at 40% ht is the one with the highest values, followed by the sample at 30% ht and finally the plasma one. This is because the presence of erythrocytes gives blood a different behavior from an aqueous solution. The higher the RBC concentration of the sample, the more viscous and less Newtonian it will be.

By performing experiments on blood samples altered with DIW, we found that the values of  $n$  (Table IV) are well below the unaltered blood sample values. We are seeing that DIW causes blood to have an even more non-Newtonian behavior. This is due to the small proportion of hemolysis that happens when the RBC is overhydrated. It increased hemoglobin in the plasma compared with the unaltered blood. The remaining cells that had not lysed increased in size, causing the apparent hematocrit to increase, leading to an increase in viscosity. From the experiments with blood altered with NaCl, the values of  $n$  (Table IV) are well above the other samples' value. Hence, we are seeing that NaCl causes blood to have a more Newtonian behavior. This is because red blood cells crenate when they are put in a hypertonic solution, leading to a decrease in the apparent hematocrit of the solution in comparison with that of the non-hemolyzed blood of the unaltered sample. The cells take up less space due to the rapid loss of water, which in turn will create a more aqueous solution, leading to more Newtonian conduct. Red blood cells crenate when put under a hypertonic solution, leading to a decrease in the hematocrit of the solution in comparison with that of the non-hemolyzed blood of the unaltered sample. This is because the cells take up less space due to the rapid loss of water, which in its turn will create a more aqueous-like, less viscous solution.<sup>26,30</sup>

The intracellular fluid of erythrocytes is a solution of salts, glucose, protein, and hemoglobin. A 0.9% NaCl solution is said to be isotonic: when blood cells reside in such a medium, the intracellular and extracellular fluids are in osmotic equilibrium across the cell membrane, and there is no net influx or efflux of water. When subjected to



hypertonic media (e.g., 1.8% NaCl), we undergo collapse (leading to crenation) due to the rapid osmotic efflux of water. The cells lose their normal biconcave shape. On the other hand, in a hypotonic environment (e.g., 0.4% NaCl or distilled water), an influx of water occurs: the cells swell, the integrity of their membranes is disrupted, allowing the escape of their hemoglobin (hemolysis), which dissolves in the external medium.<sup>31</sup> When we compared the results for the differently altered samples with the non-modified one, it was seen that the viscosity of the DIW altered sample is the one with the highest values, followed by the sample at 40% ht and, finally, the NaCl altered one. The addition of DIW provoked an apparent hematocrit increase, while the addition of NaCl caused a decrease in respect to the non-altered blood samples. Both samples had the same initial erythrocyte concentration.<sup>29</sup> These results are in accordance with previous experiments as well as with the homeostatic theory. Therefore, we can say that our model and setup allow for a good differentiation between these three different homeostatic phases (equilibrium, hypotonic, and hypertonic), which is a positive result for the first step to differentiate human pathologies using rheological measurements.

## ACKNOWLEDGMENTS

The authors thank Rheo Dx. for making this research possible.

C.R.-L. received funding from the Doctorat Industrial (2021 DI 064) program from AGAUR (Generalitat de Catalunya) as well as the 2021 Student collaboration scholarship at a research group given by the Institute of Nanoscience and Nanotechnology (IN2UB). LM-M received funding from the Doctorat Industrial (2018 DI 068) program from AGAUR (Generalitat de Catalunya). AH-M acknowledges funding under Project PID2019-106063GB-I00 and AGAUR (Generalitat de Catalunya) under Project 2021 SGR00450.

## AUTHOR DECLARATIONS

### Conflict of Interest

The authors have no conflicts to disclose.

### Author Contributions

**Carla Riera-Llobet:** Conceptualization (equal); Data curation (lead); Formal analysis (lead); Investigation (lead); Writing – original draft (lead); Writing – review & editing (lead). **Lourdes Mendez-Mora:** Investigation (equal); Writing – review & editing (lead). **Maria Cabello-Fusares:** Writing – review & editing (equal). **Aurora Hernández-Machado:** Conceptualization (lead); Methodology (lead); Supervision (equal); Writing – review & editing (equal).

## DATA AVAILABILITY

The data that support the findings of this study are available from the corresponding author upon reasonable request.

## REFERENCES

- G. M. Whitesides, “The origins and the future of microfluidics,” *Nature* **442**(7101), 368–373 (2006).
- T. M. Squires and S. R. Quake, “Microfluidics: Fluid physics at the nanoliter scale,” *Rev. Mod. Phys.* **77**(3), 977–1026 (2005).
- C. Tropea, *Handbook of Experimental Fluid Mechanics* (Springer, Berlin, Heidelberg, 2007).
- D. Bartolo and D. G. A. L. Aarts, “Microfluidics and soft matter: Small is useful,” *Soft Matter* **8**(41), 10530–10535 (2012).
- S. A. Vanapalli, M. H. G. Duits, and F. Mugele, in *Biomicrofluidics* (American Institute of Physics Inc., 2009).
- Y. Kawano, C. Otsuka, J. Sanzo, C. Higgins, T. Nirei, T. Schilling, and T. Ishikawa, “Expanding imaging capabilities for microfluidics: applicability of Darkfield Internal Reflection Illumination (DIRI) to observations in microfluidics,” *PLoS One* **10**(3), e0116925 (2015).
- J. Atencia and D. J. Beebe, “Controlled microfluidic interfaces,” *Nature* **437**(7059), 648–655 (2005).
- R. Paton, *Incompressible Flow* (Wiley, 2013).
- N. Srivastava, R. D. Davenport, and M. A. Burns, “Nanoliter viscometer for analyzing blood plasma and other liquid samples,” *Anal. Chem.* **77**(2), 383–392 (2005).
- G. Tomaiuolo, “Biomechanical properties of red blood cells in health and disease towards microfluidics,” *Biomicrofluidics* **8**(5), 051501 (2014).
- O. K. Baskurt and H. J. Meiselman, “Blood rheology and hemodynamics,” *Semin. Thromb. Hemostasis* **29**(5), 435–450 (2003).
- B. Fan, X. Li, D. Chen, H. Peng, J. Wang, and J. Chen, “Development of microfluidic systems enabling high-throughput single-cell protein characterization,” *Sensors* **16**(2), 232 (2016).
- G. N. B. Jackson, K. J. Ashpole, and S. M. Yentis, “The TEG® vs the ROTEM® thromboelastography/thromboelastometry systems,” *Anaesthesia* **64**(2), 212–215 (2009).
- S. A. H. M. Van Den Tillaart, M. P. H. Busard, and J. B. M. Z. Trimbois, “The use of distilled water in the achievement of local hemostasis during surgery,” *Gynecol. Surg.* **6**(3), 255–259 (2009).
- F. Behroozi, “A fresh look at the Young-Laplace equation and its many applications in hydrostatics,” *Phys. Teach* **60**(5), 358–361 (2022).
- G. B. Thurston and E. B. Gaertner, “Viscoelasticity of electrorheological fluids during oscillatory flow in a rectangular channel,” *J. Rheol.* **35**(7), 1327–1343 (1991).
- C. Trejo-Soto, E. Costa-Miracle, I. Rodríguez-Villarreal, J. Cid, M. Castro, T. Alarcón, and A. Hernández-Machado, “Front microrheology of the non-Newtonian behaviour of blood: Scaling theory of erythrocyte aggregation by aging,” *Soft Matter* **13**(16), 3042–3047 (2017).
- L. Méndez-Mora, M. Cabello-Fusares, J. Ferré-Torres, C. Riera-Llobet, S. Lopez, C. Trejo-Soto, T. Alarcón, and A. Hernández-Machado, “Microrheometer for biofluidic analysis: Electronic detection of the fluid-front advancement,” *Micromachines* **12**(6), 726 (2021).
- C. A. Trejo Soto, E. Costa Miracle, Á. I. Rodríguez Villarreal, J. Cid Vidal, M. Castro Ponce, T. Alarcón Cor, and A. Hernández-Machado, “Front microrheology of biological fluids,” *J. Phys. Conf. Ser.* **1043**, 012058 (2018).
- M. Queral-Martín, M. Pradas, R. Rodríguez-Trujillo, M. Arundell, E. Corvera Poiré, and A. Hernández-Machado, “Pinning and avalanches in hydrophobic microchannels,” *Phys. Rev. Lett.* **106**(19), 194501 (2011).
- V. L. Lew and T. Tiffert, “On the mechanism of human red blood cell longevity: Roles of calcium, the sodium pump, PIEZO1, and Gardos Channels,” *Front. Physiol. Physiol.* **8**, 977 (2017).
- E. Llaudet-Planas, J. L. Vives-Corróns, V. Rizzuto, P. Gómez-Ramírez, J. Sevilla Navarro, M. T. Coll Sibina, M. García-Bernal, A. Ruiz Llobet, I. Badell, P. Velasco-Puyó, J. L. Dapena, and M. M. Mañú-Pereira, “Osmotic gradient ektacytometry: A valuable screening test for hereditary spherocytosis and other red blood cell membrane disorders,” *Int. J. Lab. Hematol.* **40**(1), 94–102 (2018).
- R. Galanello and R. Origa, “Beta-thalassemia,” *Orphanet J. Rare Dis.* **5**, 11 (2010).
- S. Payán-Pernía, E. Krishnevskaya, I. Hernández-Rodríguez, Á. F. Remacha Sevilla, Á. Ancochea Serra, C. Morales-Indiano, M. Serra Ferrer, and J. L. Vives-Corróns, “Distinguishing iron deficiency from beta-thalassemia trait by new generation ektacytometry,” *Int. J. Lab. Hematol.* **43**(2), e58–e60 (2021).
- R. Huisjes, A. Bogdanova, W. W. van Solinge, R. M. Schiffelers, L. Kaestner, and R. van Wijk, “Squeezing for life—Properties of red blood cell deformability,” *Front. Physiol.* **9**, 656 (2018).

- <sup>26</sup>O. Nepal and J. P. Rao, “Haemolytic effects of hypo-osmotic salt solutions on human erythrocytes,” *Kathmandu Univ. Med. J.* **9**(34), 35–39 (2012).
- <sup>27</sup>C. Trejo-Soto, E. Costa-Miracle, I. Rodriguez-Villarreal, J. Cid, T. Alarcón, and A. Hernández-Machado, “Capillary filling at the microscale: Control of fluid front using geometry,” *PLoS One* **11**(4), e0153559 (2016).
- <sup>28</sup>L. Kaestner and A. Bogdanova, “Regulation of red cell life-span, erythropoiesis, senescence, and clearance,” *Front. Physiol.* **5**, 269 (2014).
- <sup>29</sup>L. Kaestner, “Cation channels in erythrocytes—Historical and future perspective,” in *Calcium Signalling* (Springer, Berlin, Heidelberg, 2013).
- <sup>30</sup>L. K. Goodhead and F. M. MacMillan, “Measuring osmosis and hemolysis of red blood cells,” *Adv. Physiol. Educ.* **41**(2), 298–305 (2017).
- <sup>31</sup>McGill Physiology, *Red Cell Fragility—Osmotic Hemolysis* (McGill Physiol. Virtual Laboratory, 2023).